Mathematics

https://www.aimspress.com/journal/Math

Research article

Shape reconstruction of acoustic obstacle with linear sampling method and neural network

Bowen Tang[1], Xiaoying Yang[1,*] and Lin Su[2]

[1] School of Mathematics and Statistics, Changchun University of Technology, 3000. Beiyuanda Ave, Changchun, Jilin 130000, China

[2] Wuxi Weintdata Technology Co. Ltd, 2. Longshan Rd, Wuxi, Jiangsu 214000, China

* **Correspondence:** Email: yangxiaoying@ccut.ecu.cn; Tel: +8643185716486.

Abstract: We consider the inverse scattering problem of reconstructing the boundary of an obstacle by using far-field data. With the plane wave as the incident wave, a priori information of the impenetrable obstacle can be obtained via the linear sampling method. We have constructed the shape parameter inversion model based on a neural network to reconstruct the obstacle. Numerical experimental results demonstrate that the model proposed in this paper is robust and performs well with a small number of observation directions.

Keywords: inverse acoustic scattering problems; linear sampling method; neural network; shape reconstruction of obstacles
Mathematics Subject Classification: 65B99, 68T07

1. Introduction

The physical or geometrical parameter inversion problem of obstacles when using the scattering data of electromagnetic waves, acoustic waves, or elastic waves often arises in the fields of radar, sonar detection, remote sensing, geophysics, medical imaging, and non-destructive testing. There is usually no continuous mutual dependence between the scattering data measured in reality and the obstacle. In the case of measurement error, the inverse obstacle scattering problem is usually ill-posed. Alessandrini and Rondi [1] and Liu and Zou [2]. successively proved the uniqueness of reconstructing obstacles by using far-field data with one incident wave under different a priori assumptions.

It is necessary to overcome the ill-posedness while solving the reconstruction problem of the obstacle. The regularization method is widely used [3]. In the past few decades, the iterative regularization method has become a standard method for solving ill-posed inverse problems. However, such methods are computationally intensive, and the choice of regularization parameters is

rather difficult. Other widely used methods [4–7] for solving inverse scattering problems include qualitative methods such as the factorization method [8] and the sampling method [9–11]. There is no need for these methods to have a priori information of the unknown obstacles. Compared with the iterative regularization methods, they are also computationally faster.

However, the methods mentioned above can only determine the approximate shape of the obstacle, rather than the accurate shape. In recent years, scholars have used neural networks to learn the mapping from measurement data to the shape of the obstacle by training sample data and using data-driven learning techniques [12–16]. As such techniques are less affected by noise, they demonstrate highly impressive results on many challenging inverse problems [17–20], such as super-resolution [21], image restoration [22], compressed sensing [23, 24], and ultrasonic tomography [25]. In [26], the scholars develop a novel reconstruction scheme that involves using plasmon resonances to investigate the shape reconstructions of sub-wavelength objects. Using the broad learning system with preprocessing, impenetrable obstacles have been reconstructed [27]. Scholars have also proposed the hybrid approach, which combines the linear sampling method (LSM) and the Bayesian method to simultaneously reconstruct multiple obstacles [28, 29]. So far, the neural network methods have been impressive in terms of reconstruction effectiveness, but their theoretical analyses are relatively scarce. Please see [30–32] for the corresponding studies.

We consider the highly accurate shape parameter inversion problem of a single impenetrable obstacle with sound-soft boundary conditions. Taking the plane wave with a finite number of incident directions as the incident waves, the LSM is used to obtain a priori information of the obstacle. A method for reconstructing the shape of the obstacle has been developed through the use of the regression neural network.

The remainder of this paper is organized as follows. In Section 2, we discuss the acoustic scattering model. In Section 3, we use the LSM to obtain a priori information and construct a shape parameter inversion model that includes the feature extraction module and the parameter inversion module. In Section 4, a variety of numerical experiments are detailed to illustrate the feasibility and convergence of the model under different conditions. In Section 5, we conclude the paper.

2. Acoustic scattering model

Consider the two-dimensional acoustic wave-scattering problem of an impenetrable obstacle $D \subset \mathbb{R}^2$ in homogeneous media, given an incident plane wave $u^i = e^{ikd \cdot x}$, where $k \in \mathbb{R}^+$ is the wave number of the incident plane wave and $d = (\cos \theta, \sin \theta)^T$ is the unit incidence direction, $\theta \in [0, 2\pi]$. The scattering problem is determined by the exterior problem of the Helmholtz equation:

$$\begin{cases} \Delta u^s + k^2 u^s = 0, & x \in \mathbb{R}^2 \backslash \bar{D}, \\ u^i + u^s = 0, & x \in \partial D, \\ \lim_{r \to \infty} r^{1/2} \left(\frac{\partial u^s}{\partial r} - iku^s \right) = 0, & r := |x|, \end{cases} \tag{2.1}$$

and the external total field of the obstacle is given by $u(x) := u^i(x) + u^s(x)$.

The scattering wave-field outside of obstacle D has the following asymptotic form at infinity:

$$u^s(x) = \frac{e^{ik|x|}}{\sqrt{|x|}} \left\{ u^\infty(\hat{x}; d, k) + O\left(\frac{1}{|x|} \right) \right\}, \quad |x| \to \infty, \tag{2.2}$$

where $\hat{x} = x/|x|$. The far-field data $u^\infty(\hat{x}; d, k)$ represents the asymptotic state of the scattering field at infinity.

Since the far-field data $u^\infty(\hat{x}; d, k)$ is related to the incident direction d and the observation direction $\hat{x}$, the following assumptions can be made.

Assumption 2.1. *The incident direction $d = (\cos\theta, \sin\theta)$, the observation direction $\hat{x} = (\cos\beta, \sin\beta)$, the incidence angle α, and the observation angle β are uniformly distributed in $[0, 2\pi)$, namely,*

$$
\begin{aligned}
\alpha &:= 2(i-1)\pi/n, \quad i = 1, 2, \cdots, n, \\
\beta &:= 2(j-1)\pi/n', \quad j = 1, 2, \cdots, n',
\end{aligned}
\tag{2.3}
$$

where n denotes the number of incident directions and n' denotes the number of observation directions.

Assumption 2.2. *Considering the case of the far-field data $u_{ij}^\infty = u^\infty\left(\hat{x}_j, d_i, k\right)$ and the plane wave with n incident directions and n' observation directions, the vector form of the far-field data is given by*

$$
(u_{11}^\infty, u_{12}^\infty, \cdots, u_{1n'}^\infty, u_{21}^\infty, \cdots, u_{2n'}^\infty, \cdots u_{n1}^\infty, \cdots, u_{nn'}^\infty) \in \mathbb{C}^{nn'}
$$

With $N = n \cdot n'$, the far-field data could be rewritten as

$$
X = (x_1, x_2, \cdots, x_N) \in \mathbb{C}^N,
$$

*where $x_{(i-1)n'+j} = u_{ij}^\infty$, $i = 1, 2, \cdots n$, $j = 1, 2, \cdots, n'$.*

Next we invert the shape parameters of the obstacle.

3. Shape parameter inversion model based on a neural network

3.1. The linear sampling method

We obtain a priori information of the obstacle by using the LSM and fit the shape parameters of the obstacle by using the least-squares method. The LSM is a simple and effective method to reconstruct the shape of an obstacle in inverse scattering problems. Theorem 4.1 in [33] forms the basis of the LSM. The LSM elegantly turns the reconstruction of the obstacle into the process of numerically determining the indicator function g. The mathematical principle and the general procedure can be found in [34–37].

We apply the peanut-shaped, the clover-shaped, and the star-shaped scatters as the examples. We obtained the far-field data with 360 incident directions and 360 observation directions. The contour map of the indicator function can be obtained by using the LSM, and we have reconstructed the shape of the obstacle. The reconstruction results are presented in Figure 1. As seen in Figure 1, the LSM is unable to accurately invert the location and the shape of the obstacle. In this paper, we indicate the obstacle boundary by inside-out selecting the second smooth curve, which can contain all branches.
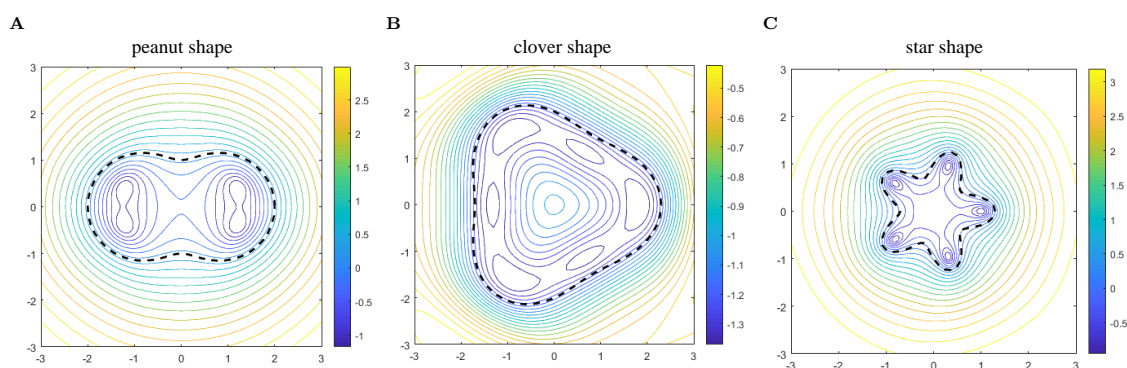
Figure 1. Contour lines of the shape reconstruction of the peanut-shaped, the clover-shaped, and the star-shaped obstacles, where the solid lines indicate the contour lines and the dashed lines indicate the real shape of the obstacle.

The parametric equations of the selected contour lines are assumed to be as follows:

$$\begin{cases} x = x(\theta), \\ y = y(\theta). \end{cases}$$

By computing the Fourier series of $(x(\theta), y(\theta))$ and truncating to the $2K + 1$-th term, we have

$$\begin{cases} x(\theta) = a_0 + \sum_{i=1}^{K} a_i \cos(i \cdot \theta) + \sum_{i=K+1}^{2K} a_i \sin((i - K) \cdot \theta), \\ y(\theta) = b_0 + \sum_{i=1}^{K} b_i \cos(i \cdot \theta) + \sum_{i=K+1}^{2K} b_i \sin((i - K) \cdot \theta). \end{cases} \tag{3.1}$$

According to (3.1), the discrete Fourier approximation method can be used to fit the contour lines and obtain the coefficients a_i and b_i, $i = 0, 1, \cdots, 2K$. In order to simplify the function form, the smaller coefficients were set to be zero. The threshold value ξ can be set such that

$$a_i = \begin{cases} a_i, & |a_i| \geq \xi, \\ 0, & |a_i| < \xi, \end{cases} \qquad b_i = \begin{cases} b_i, & |b_i| \geq \xi, \\ 0, & |b_i| < \xi, \end{cases}$$

Then, the approximate expression for contour lines can be obtained.

Taking Figure 1A as an example, we set $K = 4$ and $\xi = 0.05$, and the corresponding fitted curve equations can be obtained by using the above methods:

$$\begin{cases} x(\theta) = a_1 \cos(\theta) + a_3 \cos(3\theta), \\ y(\theta) = b_5 \sin(\theta) + b_7 \sin(3\theta), \end{cases} \tag{3.2}$$

where $a_1 = 1.724$, $a_3 = 0.2369$, $b_3 = 1.209$, $b_7 = 0.2786$. The fitting results for the contour lines selected from Figure 1A to C are shown in Figure 2A–C, respectively.
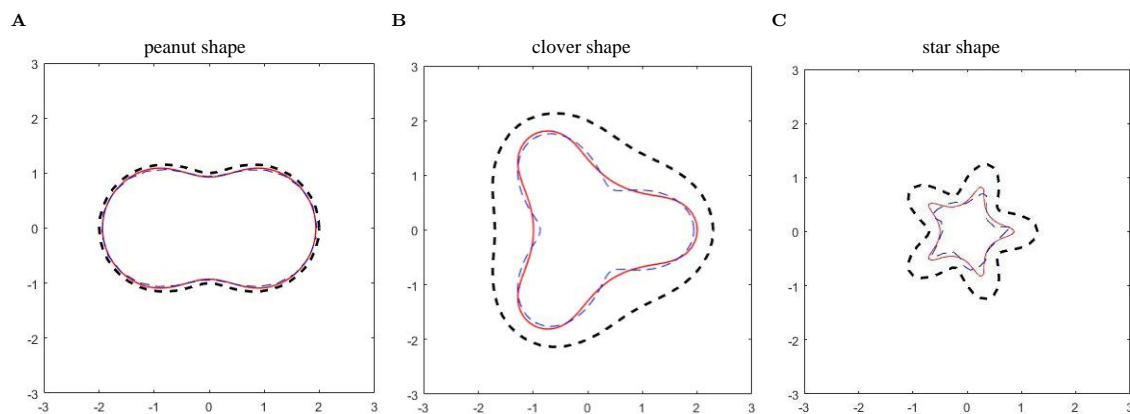
Figure 2. The contour fitting results for the peanut-shaped, the clover-shaped, and the star-shaped obstacles, where the blue dotted lines indicate the selected contours, the black dotted lines indicate the real obstacles, and the red solid lines indicate the fitted curves.

Therefore, the shape reconstruction of the obstacle can be transformed into the inversion of the shape parameters. The inverse obstacle scattering problem in Figure 1A is to determine the shape parameters denoted $Y = (a_1, a_3, b_5, b_7)$ from the far-field data $X = (x_1, x_2, ..., x_N)$.

3.2. Extraction of far-field features

Without loss of generality, it may be assumed that the obstacle has M shape parameters, denoted as

$$Y = (y_1, y_2, \cdots, y_M) \in \mathbb{R}^M.$$

We next introduce two operator symbols that are used in the shape parameter inversion model in [38].

1) Let $A = (a_{ij})$ denote a matrix in $n \times m$ and $B = (b_{ij})$ denote a matrix in $p \times m$; then, $[A, B]$ denotes the matrix splicing:

$$[A, B] = \begin{pmatrix} a_{11} & a_{12} & \cdots & a_{1m} \\ & & \cdots & \\ a_{n1} & a_{n2} & \cdots & a_{nm} \\ b_{11} & b_{12} & \cdots & b_{1m} \\ & & \cdots & \\ b_{p1} & b_{p2} & \cdots & b_{pm} \end{pmatrix} \in \mathbb{R}^{(n+p) \times m}.$$

2) Let $A = (a_{ij}) \in \mathbb{R}^{m \times n}$ and $B = (b_{ij}) \in \mathbb{R}^{m \times n}$ both denote matrices in $n \times m$; then, $A * B$ denotes the Hadamard product:

$$A * B = (a_{ij} b_{ij}) \in \mathbb{R}^{m \times n},$$

Particularly, we denote $A * A = A^2$ in the case of $A = B$.

For the purpose of calculations, we rewrite $x_t = a_t + ib_t$ as $x_t = (a_t, b_t)^T$, $t = 1, 2, \cdots, N$, and the far-field data can be given by $X = (x_1, x_2, \cdots, x_N) \in \mathbb{R}^{2 \times N}$. Based on the spatial relationship between the far-field data and the interaction between the shape parameters, we chose to use a memory-enabled neural network which can propagate information in the time dimension. The shape parameter

inversion model based on a neural network (SPINN) model was constructed to invert the parameter $\tilde{Y} = (\tilde{y}_1, \tilde{y}_2, \cdots, \tilde{y}_M) \in \mathbb{R}^M$. As illustrated in Figure 3, the left side represents the feature extraction module, and the right side represents the parameter inversion module.
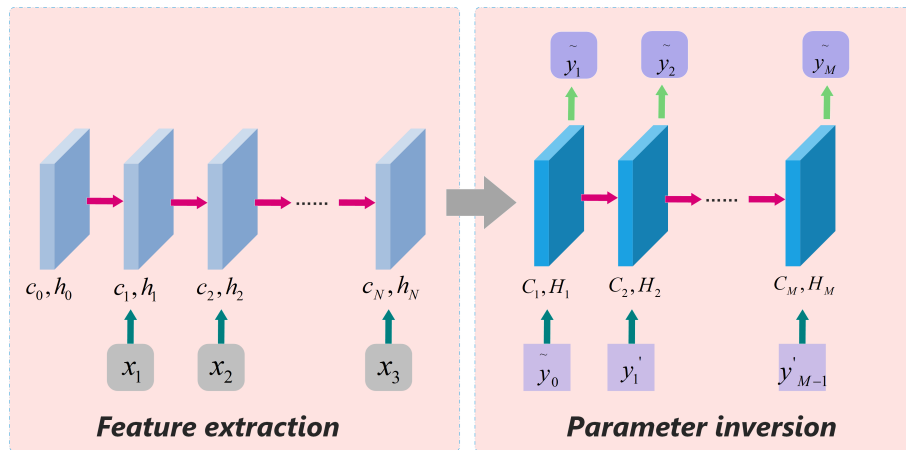
Figure 3. The structure of the SPINN model.

The feature extraction module uses gating thought to extract the long-term features $c_N \in \mathbb{R}^m$ and the short-term features $h_N \in \mathbb{R}^m$. Let $X = (x_1, x_2, \cdots, x_N) \in \mathbb{R}^{2 \times N}$ be the input values and $c_t \in \mathbb{R}^m$ be the long-term features, including the first t components of the far-field data, $t = 1, 2, \cdots, N$. $h_t \in \mathbb{R}^m$ denotes the current feature of the t-th component. We initialized c_0 and d_0 to be zero matrices. The far-field features c_t and d_t can be extracted from each component of the far-field data by using the long short-term memory (LSTM) gating structure presented in Figure 4. The features are calculated as follows:

$$h_t = o_t * L(c_t), \tag{3.3}$$

$$c_t = (f_t * c_{t-1}) + (i_t * z_t), \tag{3.4}$$

where the forget gate $f_t \in \mathbb{R}^m$ controls the information quantity from c_t into c_{t-1}, the input gate $i_t \in \mathbb{R}^m$ controls the information quantity from $z_t \in \mathbb{R}^m$ into c_{t-1}, and the output gate $o_t \in \mathbb{R}^m$ controls the information quantity from h_t into c_t. For the sake of convenience, we set the bias to be a zero vector, namely, $b = (0, 0, \cdots, 0)^T$. In order to increase the nonlinearity of the model, f_t, i_t, z_t, o_t could respectively be defined as follows:

$$f_t = \sigma\left(w_{fi}x_t + w_{fh}h_{t-1}\right), \tag{3.5}$$

$$i_t = \sigma\left(w_{ix}x_t + w_{ih}h_{t-1}\right), \tag{3.6}$$

$$z_t = L\left(w_{zx}x_t + w_{zh}h_{t-1}\right), \tag{3.7}$$

$$o_t = \sigma\left(w_{ox}x_t + w_{oh}h_{t-1}\right), \tag{3.8}$$

where L is a hyperbolic tangent function and σ is the sigmoid function. $w_{ox}, w_{fx}, w_{ix}, w_{xx} \in \mathbb{R}^{m \times 2}$ denote the weights of x_t and the hidden layer in o_t, f_t, i_t, z_t, respectively. $w_{oh}, w_{fh}, w_{ih}, w_{zh} \in \mathbb{R}^{m \times m}$ denote the weights of h_t and the hidden layer in o_t, f_t, i_t, z_t, respectively. c_N and h_N contain all component features of the far-field data, and they can be obtained after the N-time feature extraction.
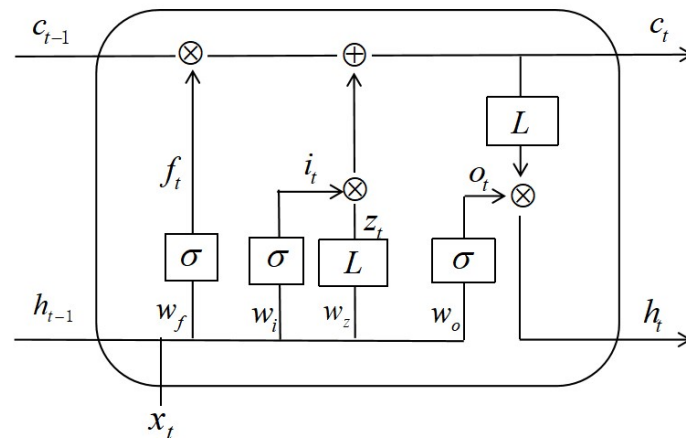
Figure 4. LSTM gating structure.

3.3. Parameter inversion

Similar to the feature extraction module, in the parameter inversion module, $H_T \in \mathbb{R}^m$ represents the current feature of the T-th component, and $C_T \in \mathbb{R}^m$ represents the long-term features of the first T components, $T = 1, 2, \cdots, M$. $\tilde{y}_T$ represents the T-th shape parameter inverted by H_T. By initializing $y'_m = 0$, $C_0 = c_N$, and $H_0 = h_N$, H_T and C_T can be calculated as follows:

$$
\begin{aligned}
H_T &= O_T * L(C_T), & C_T &= (F_T * C_{T-1}) + (I_T * Z_T), \\
F_T &= \sigma\left(W_{Fy}y'_{T-1} + W_{FH}H_{T-1}\right), & I_T &= \sigma\left(W_{Iy}y'_{T-1} + W_{IH}H_{T-1}\right), \\
Z_T &= L\left(W_{Zy}y'_{T-1} + W_{ZH}H_{T-1}\right), & O_T &= \sigma\left(W_{Oy}y'_{T-1} + W_{OH}H_{T-1}\right),
\end{aligned}
$$

where O_T, F_T, I_T, Z_T respectively represent the output gate, the forget gate, the input gate, and the input value. $W_{Oy}, W_{Fy}, W_{Iy}, W_{Zy} \in \mathbb{R}^{m \times 2}$ respectively represent the weights of y'_{T-1} and the hidden layer in O_T, F_T, I_T, Z_T. $W_{OH}, W_{FH}, W_{IH}, W_{ZH} \in \mathbb{R}^{m \times m}$ respectively represent the weights of H_{T-1} and the hidden layer in O_T, F_T, I_T, Z_T.

It is noteworthy that, for the parameter inversion, during the training process, we set $y'_T = y_T$. During the testing process with y_T unknown, $\tilde{y}_T$ can be used as an approximation of y_T, namely, $y'_T = \tilde{y}_T$.

Considering that $H_T \in \mathbb{R}^m$ and $\tilde{y}_T \in \mathbb{R}$, we can invert H_T to the T-th shape parameter $\tilde{y}_T$ by applying a full connection with an output dimension of one,

$$
\tilde{y}_T = W_D^T \cdot H_T, \tag{3.9}
$$

where $W_D \in \mathbb{R}^m$ represents the full connection weights of H_T and $\tilde{y}_T$. After M time steps, all shape parameters $Y = (\tilde{y}_1, \tilde{y}_2, \cdots, \tilde{y}_M) \in \mathbb{R}^M$ can be inverted.

3.4. SPINN model parameter update method

$X^j = (x_1^j, x_2^j, \cdots, x_N^j)$ denotes the far-field data of the j-th sample, $Y^j = (y_1^j, y_2^j, \cdots, y_M^j)$ denotes the real shape parameters of the j-th sample, and $\tilde{Y}_j = (\tilde{y}_1^j, \tilde{y}_2^j, \cdots, \tilde{y}_M^j)$ denotes the shape parameter by inverting, where $j = 1, 2, \cdots, J$. Here, J is the total number of samples.

We set

$$X_T = \left(X_T^1, X_T^2, \cdots, X_T^J\right)^T, \quad T = 1, 2, \cdots, N,$$

$$\psi_T = \left(y_T^1, y_T^2, \cdots, y_T^J\right)^T, \quad T = 1, 2, \cdots, M,$$

$$\tilde{\psi}_T = \left(\tilde{y}_T^1, \tilde{y}_T^2, \cdots, \tilde{y}_T^J\right)^T, \quad T = 1, 2, \cdots, M.$$

Define the following error function:

$$E\left(\psi_T, \tilde{\psi}_T\right) = \frac{1}{2} \sum_{T=1}^{M} \left\|\psi_T - \tilde{\psi}_T\right\|^2, \tag{3.10}$$

where $\|\cdot\|$ denotes the Euclidean norm. Noting that

$$w_e = (w_x, w_h) = \begin{pmatrix} w_{ox} & w_{fi} & w_{ix} & w_{zx} \\ w_{oh} & w_{fh} & w_{th} & w_{zh} \end{pmatrix}^T,$$

$$W_d = (W_Y, W_H) = \begin{pmatrix} W_{Oy} & W_{Fy} & W_W & W_{Zy} \\ W_{OH} & W_{FH} & W_{IH} & W_{ZH} \end{pmatrix}^T,$$

the model parameters are updated by using the gradient method. For $l = 0, 1, 2, ...$, we randomly initialize the weight $W^{(0)}$ as follows:

$$W^{(l+1)} = W^{(l)} + \Delta W^{(l)}, \tag{3.11}$$

$$\Delta W^{(l)} = -\eta \frac{\partial E^{(l)}}{\partial W^{(l)}},$$

where $W^{(l)}$ denotes the weight generated by the model in the l-th iteration update, $E^{(l)}$ denotes the error, and η denotes the learning rate.

4. Numerical experiments

We chose to apply the class of obstacle boundary curves estimated by the LSM as the examples to verify the performance of the proposed method. Thus, we have

$$\begin{cases} x(\theta) = a_1 \cos(\theta) + a_3 \cos(3\theta), \\ y(\theta) = b_5 \sin(\theta) + b_7 \sin(3\theta), \end{cases}$$

and the shape parameter $Y = (a_1, a_3, b_5, b_7) \in \mathbb{R}^4$.

J is the number of the experimental samples $(X_j, Y_j)_{j=1}^J$, $j = 1, 2, \cdots, J$. X_j denotes the far-field data of the j-th experimental sample, and Y_j denotes the corresponding shape parameters. They constitute the data set of the inversion model given by

$$Q = \left\{ \left(X_j, Y_j\right) \mid X_j \in \mathbb{R}^{2 \times N}, Y_j \in \mathbb{R}^4, j = 1, 2, \cdots, J \right\}.$$

4.1. Experimental setting

The standardized data set has been divided into the training set and the test set at the ratio of $9 : 1$. The numerical experiments were trained on the training set in a small batch mode. The size of the batch was v, $1 < v < J$. As given in Table 1, the hyperparameters of the inversion model were derived from a large number of experiments. In the following part of the paper, we fix the wave number $k = 1.5$. We used Python as the programming language.

Table 1. The hyperparameters of the SPINN model.

Hyperparameters	m	v	Iterations
Value	256	1000	100

4.2. Effect of learning rate on convergence

While using the gradient method to train the model parameters, we need to take the effect of the learning rate η into account to make the method converge quickly.

The steady sound-field was generated by a plane wave with a single incident direction. We observed it in n' directions and applied the observation angle $\alpha = \left\{0, \frac{2\pi}{n}, \cdots, \frac{2(n-1)\pi}{n}\right\}$. For the case of $n' = 35$ and the learning rates $\eta = 10^{-1}, \eta = 10^{-3}$, and $\eta = 10^{-5}$, the reconstruction results for the obstacles are shown in Figure 5A–C. Figure 6A–C show the error-iteration images with the learning rates $\eta = 10^{-1}, \eta = 10^{-3}$, and $\eta = 10^{-5}$, respectively, where the horizontal axis represents the iterations and the vertical axis represents the error values.
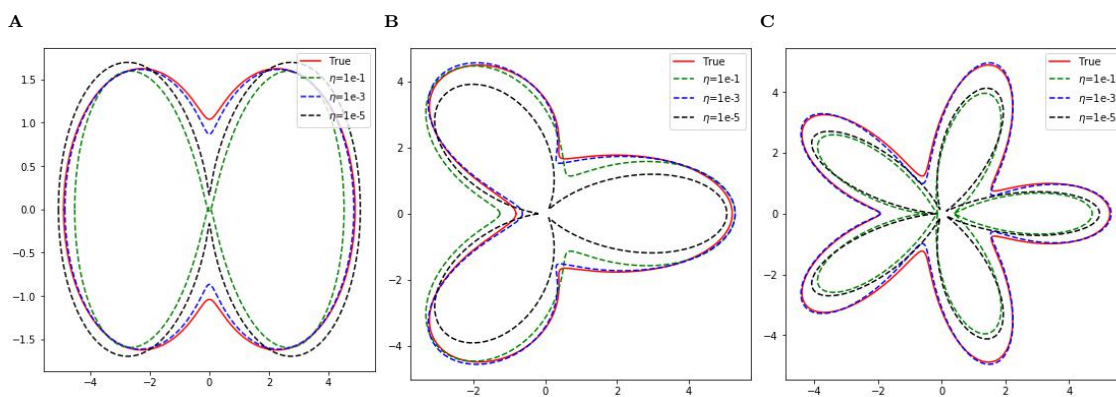
Figure 5. The reconstruction results for the peanut-shaped, the clover-shaped, and the star-shaped obstacles with different learning rates.

According to Figure 6A–C, in the case of the learning rate $\eta = 10^{-1}$, a large gradient resulted in a large update range each time. Thus, the method has no convergence and less desirable inversion. In the case of $\eta = 10^{-3}$, the range of each weight update is appropriate and the method can converge quickly. According to Figure 6B, it is known that the proposed method has superior convergence. In the case of $\eta = 10^{-5}$, the range of each weight update is so small that the model is less optimized by self-learning. The method is unable to achieve a good representation within relatively fewer iterations,

and the inversion is not satisfactory. Consequently, in the following experiments, we chose to fix the learning rate $\eta = 10^{-3}$.
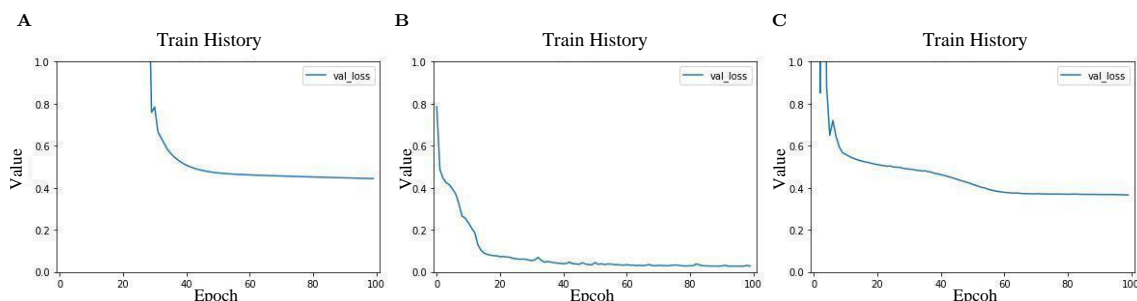
Figure 6. The error-iteration images for the clover-shaped obstacle with the learning rates $\eta = 10^{-1}, \eta = 10^{-3}$, and $\eta = 10^{-5}$.
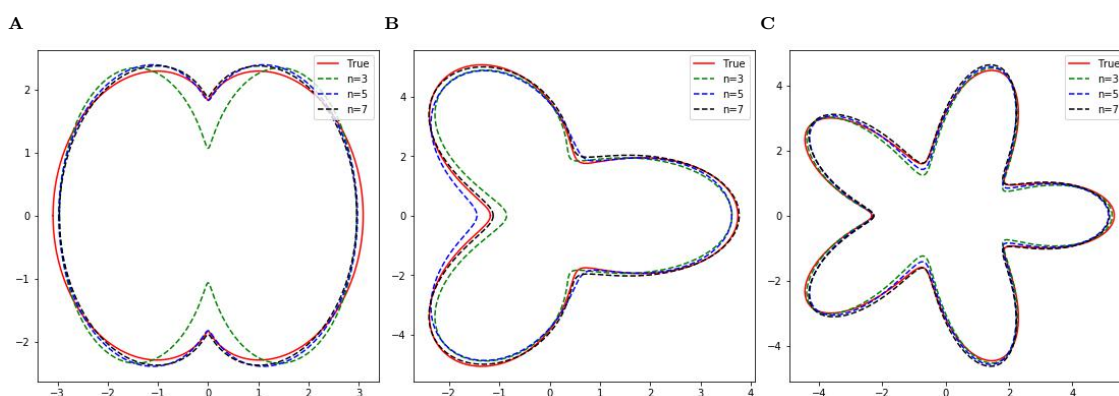
4.3. Reconstruction of the obstacles

In this subsection, we present simulations of the convergence and inversion effect of the SPINN model in different realistic scenarios.

Example 1. Reconstruct the obstacles with n incident directions and n observation directions, and there is no noise in the far-field measurement.

We set $n = 3, n = 5, n = 7$, the incidence angle $\alpha = \left\{0, \frac{2\pi}{n}, \cdots, \frac{2(n-1)\pi}{n}\right\}$, and the wave number $k = 1.5$. The observation angle could be the same as the incident angle.

The reconstruction results for the obstacles are shown in Figure 7A–C. Figure 8A–C are the error-iteration images of the peanut-shaped, clover-shaped, and star-shaped obstacles, respectively. Table 2 presents the mean square error of the inversion parameters, as obtained by using the validation set corresponding to Figure 7A.

Figure 7. The reconstruction results for the peanut-shaped, the clover-shaped, and the star-shaped obstacles with n incident directions and n observation directions.
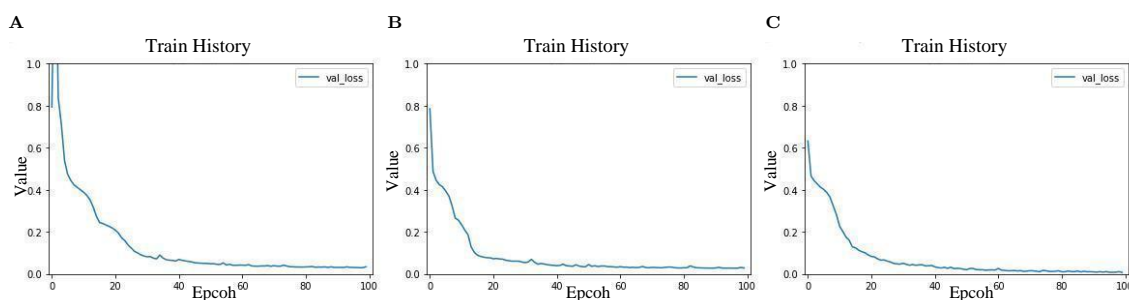
Figure 8. The error-iteration images with the learning rates $\eta = 10^{-1}, \eta = 10^{-3}$, and $\eta = 10^{-5}$. $n = 7$.

Table 2. The mean square error results obtained by reconstructing the peanut-shaped obstacle with n incident directions and n observation directions.

n	3	5	7
MSE of training data sets	0.0555	0.0339	0.0297
MSE of test data sets	0.0581	0.0368	0.0206

Figure 7 and Table 2 illustrate that, with increases in incident direction and observation direction, more far-field information is obtained, the inversion error is reduced, and the reconstruction effect of the obstacle is promoted. In the case of $n \geq 5$, the method proposed in this paper can achieve a better reconstruction effect. It can be ascertained from Figure 8 that the error function first decreases and eventually becomes stable, which indicates the convergence of the model.
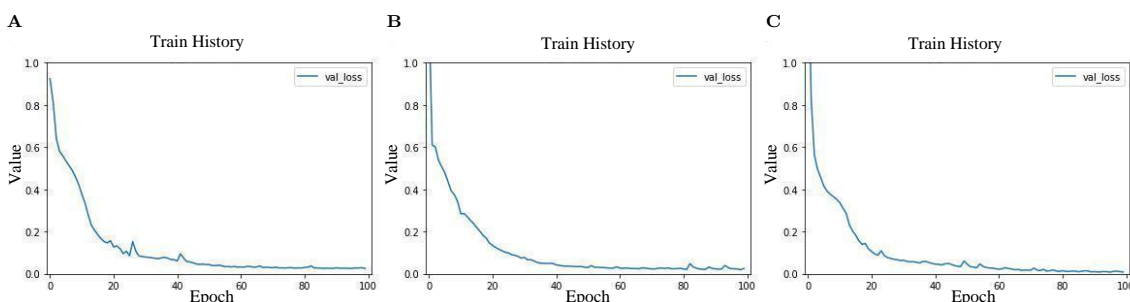
Example 2. Reconstruct the obstacles with a single incident direction and n' observation directions, and there is no noise in the far-field measurement.

Since, in the actual measurements, only a single incident direction can be used, we applied the incident direction $d = (1, 0)$, the wave number $k = 1.5$, the number of observation directions $n' = 15$, $n' = 25$, and $n' = 35$, and the observation angle $\beta = \left\{0, \frac{2\pi}{n'}, \cdots, \frac{2(n-1)\pi}{n'}\right\}$. The reconstruction results for the obstacles are shown in Figure 9. Figure 10 shows the error-iteration images for the peanut-shaped, clover-shaped, and star-shaped obstacles with one incident direction and 35 observation.

The mean square error of the shape parameter inversion is shown in Table 3. According to Figure 9 and Table 3, with an increase of n', the far-field information increases; thus, the mean square error decreases and the obstacle reconstruction effect improves. It can be ascertained from Figure 10 that, with only one incident direction and 35 observation directions, the method proposed in this paper can quickly converge and accurately invert the shape parameters.
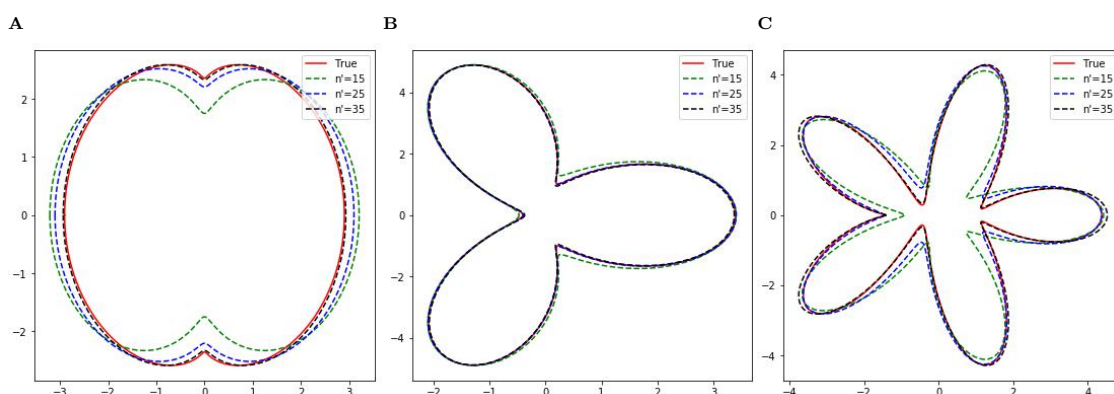
Figure 9. The reconstruction results for the peanut-shaped, the clover-shaped, and the star-shaped obstacles with one single incident direction and n' observation directions.

Figure 10. The error-iteration images with one single incident direction and 35 observation directions.

Table 3. Mean square error results obtained by reconstructing the peanut-shaped obstacle with different observation directions.

n'	15	25	35
MSE of training data sets	0.0686	0.0445	0.0230
MSE of test data sets	0.0495	0.0368	0.0186

Example 3. Reconstruct the obstacles with n incident directions and n observation directions, and there is multiplicative noise in the far-field measurement.

It is known from Example 1 that, when the numbers of incident and observation directions are both 7, the obstacles can be reconstructed well. In the actual measurement, the far-field data often contain certain measurement errors. In order to illustrate the inversion effect of the model, we applied $n = 7$, the incidence angle $\alpha = \left\{0, \frac{2\pi}{n}, \cdots, \frac{2(n-1)\pi}{n}\right\}$, and the wave number $k = 1.5$. The observation angle could be the same as the incidence angle. The far-field data contain different levels of multiplicative Gaussian noise ε. The reconstruction results for the obstacle are shown in Figure 11A–C. Figure 12 shows the error-iteration images for the peanut-shaped, clover-shaped, and star-shaped obstacles at

a far-field noise level of 30%. Table 3 shows the mean square error of the inversion parameters, as obtained by using the test set corresponding to Figure 9A.

From Figure 11A–C and Table 4, we can know that the SPINN model can perform better if the level of multiplicative Gaussian noise is less than 30%. This is because the method trains the real shape parameters and the far-field data by using measurement errors. It approximates the mapping between the far-field data and the real shape parameters, and reduces the impact of measurement errors on the inversion effect. Even if the measured noise level in the far-field data reaches 50%, the SPINN method can still roughly invert the shape parameters of the obstacle. Figure 12 illustrates that the SPINN model still converges well.
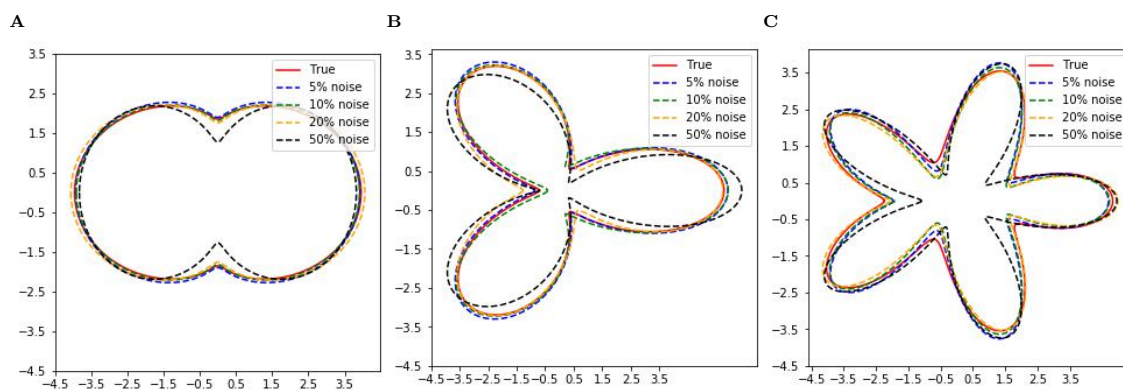
Figure 11. The reconstruction results for the peanut-shaped, the clover-shaped, and the star-shaped obstacles with noise in the far-field measurement.
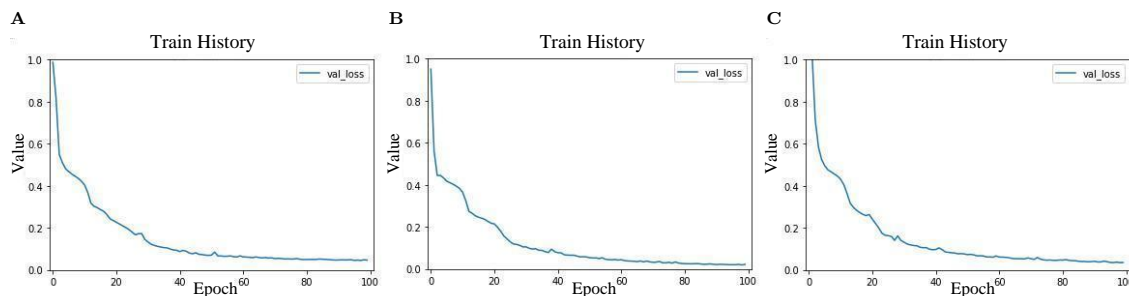
Figure 12. The error-iteration images with 30% far-field noise level.

Table 4. Mean square error results obtained by reconstructing the peanut-shaped obstacle with noise in the far-field measurement.

Noise level	5%	10%	30%	50%
MSE of training data sets	0.0207	0.0314	0.0473	0.0723
MSE of test data sets	0.0392	0.0410	0.0527	0.0892

In the numerical experiments, we first investigated the influence of different learning rates on the convergence of the SPINN model; we then determined the learning rate for the subsequent experiments.

Numerical experiments show that the proposed method converges and yields better results in the case of small numbers of incident directions and observation directions. In particular, when the incident wave has only one incident direction, by increasing the number of observation directions, the method converges and can reconstruct the shape of the obstacle more accurately. In addition, Example 3 shows the convergence of the method proposed in this paper in the case of low noise; it also shows the robustness of the model.

5. Conclusions

In this study, we have used the LSM to obtain a priori information of the obstacle and construct the SPINN model to invert the shape parameters. In the numerical experiments, the effect of hyperparameters on the convergence of the model was evaluated. It was shown that the method is suitable for the case of small numbers of incident directions and observation directions, and it is also suitable for the case of one single incident direction and multiple observation directions. It also applies to the inverse obstacle scattering problem with noise data. The method proposed in this paper converged in all of the experiments.

Use of AI tools declaration

The authors declare they have not used Artificial Intelligence (AI) tools in the creation of this article.

Acknowledgments

Conflict of interest

All authors declare no conflicts of interest in this paper.

References

1. G. Alessandrini, L. Rondi, Determining a sound-soft polyhedral scatterer by a single far-field measurement, *Proc. Amer. Math. Soc.*, **133** (2005), 1685–1691.

2. H. Liu, J. Zou, Uniqueness in an inverse acoustic obstacle scattering problem for both sound-hard and sound-soft polyhedral scatterers, *Inverse Probl.*, **22** (2006), 515–524. http://doi.org/10.1088/0266-5611/22/2/008

3. O. Ivanyshyn, R. Kress, Nonlinear integral equations in inverse obstacle scattering, *Mathematical Methods in Scattering Theory and Biomedical Engineering*, **51** (2006), 39–50. https://doi.org/10.1142/9789812773197_0005

4. J. Li, H. Liu, *Numerical methods for inverse scattering problems*, Singapore: Springer, 2023. https://doi.org/10.1007/978-981-99-3772-1

5. H. Diao, H. Liu, *Spectral geometry and inverse scattering theory*, Cham: Springer, 2023. https://doi.org/10.1007/978-3-031-34615-6

6. L. Borcea, H. Kang, H. Liu, G. Uhlmann, *Inverse problems and imaging*, panoramas et Syntheses, 2015.

7. J. Li, H. Liu, J. Zou, An efficient multilevel algorithm for inverse scattering problem, In: *Advances in computation and intelligence*, Berlin, Heidelber: Springer, 2007, 234–242. https://doi.org/10.1007/978-3-540-74581-5_25

8. J. Xiang, G. Yan, The factorization method for a mixed inverse elastic scattering problem, *IMA. J. Appl. Math.*, **87** (2022), 407–437. http://doi.org/10.1093/imamat/hxac010

9. J. Wang, B. Chen, Q, Yu, Y. Sun, A novel sampling method for time domain acoustic inverse source problems, *Phys. Scr.*, **99** (2024), 035221. http://doi.org/10.1088/1402-4896/ad21c7

10. D. Colton, A. Kirsch, A simple method for solving inverse scattering problems in the resonance region, *Inverse Probl.*, **12** (1996), 383–393. http://doi.org/10.1088/0266-5611/12/4/003

11. J. Li, J. Yang, B. Zhang, A linear sampling method for inverse acoustic scattering by a locally rough interface, *Inverse Probl. Imag.*, **15** (2021), 1247–1267. http://doi.org/10.3934/ipi.2021036

12. Y. Gao, H. Liu, X. Wang, K. Zhang, On an artificial neural network for inverse scattering problems, *J. Comput. Phys.*, **448** (2021), 110771. http://doi.org/10.1016/j.jcp.2021.110771

13. W. Yin, Z. Yang, P. Meng, Solving inverse scattering problem with a crack in inhomogeneous medium based on a convolutional neural network, *Symmetry*, **15** (2023), 119. https://doi.org/10.3390/sym15010119

14. P. Zhang, P. Meng, W. Yin, H. Liu, A neural network method for time-dependent inverse source problem with limited-aperture data, *J. Comput. Appl. Math.*, **421** (2023), 114842. https://doi.org/10.1016/j.cam.2022.114842

15. W. Yin, J. Ge, P. Meng, F. Qu, A neural network method for the inverse scattering problem of impenetrable cavities, *Electron. Res. Arch.*, **28** (2020), 1123–1142. https://doi.org/10.3934/era.2020062

16. W. Yin, W. Yang, H. Liu, A neural network scheme for recovering scattering obstacles with limited phaseless far-field data, *J. Comput. Phys.*, **417** (2020), 109594. https://doi.org/10.1016/j.jcp.2020.109594

17. H. Liu, C. Mou, S. Zhang, Inverse problems for mean field games, *Inverse Probl.*, **39** (2023), 085003. https://doi.org/10.1088/1361-6420/acdd90

18. Y. He, H. Liu, X. Wang, A novel quantitative inverse scattering scheme using interior resonant modes, *Inverse Probl.*, **39** (2023), 085002. https://doi.org/10.1088/1361-6420/acdc49

19. X. Cao, H. Diao, H. Liu, J. Zou, Two single-measurement uniqueness results for inverse scattering problems within polyhedral geometries, *Inverse Probl. Imag.*, **16**, (2022), 1501–1528. https://doi.org/10.3934/ipi.2022023

20. X. Cao, H. Diao, H. Liu, J. Zou, On nodal and singular structures of Laplacian eigenfunctions and applications to inverse scattering problems, *J. Math. Pures Appl.*, **143** (2020), 116–161. https://doi.org/10.1016/j.matpur.2020.09.011

21. L. Liu, W. Liu, D. Teng, Y. Xiang, F.-Z. Xuan, A multiscale residual U-net architecture for super-resolution ultrasonic phased array imaging from full matrix capture data, *J. Acoust. Soc. Am.*, **154** (2023), 2044–2054. http://doi.org/10.1121/10.0021171

22. A. Reed, T. Blanford, D. Brown, S. Jayasuriya, SINR: Deconvolving circular sas images using implicit neural representations, *IEEE J. Sel. Topics Signal Process.*, **17** (2023), 458–472. http://doi.org/10.1109/JSTSP.2022.3215849

23. W. Yu, X. Huang, Reconstruction of aircraft engine noise source using beamforming and compressive sensing, *IEEE Access*, **6** (2018), 11716–11726. http://doi.org/10.1109/ACCESS.2018.2801260

24. T. Nagata, K. Nakai, K. Yamada, Y. Saito, T. Nonomura, M. Kano, et al., Seismic wavefield reconstruction based on compressed sensing using data-driven reduced-order model, *Geophys. J. Int.*, **233** (2023), 33–50. http://doi.org/10.1093/gji/ggac443

25. M. Suhonen, A. Pulkkinen, T. Tarvainen, Single-stage approach for estimating optical parameters in spectral quantitative photo acoustic tomography, *Journal of the Optical Society of America A*, **41** (2024), 527–542. http://doi.org/10.1364/JOSAA.518768

26. M. Ding, H. Liu, G. Zheng, Shape reconstructions by using plasmon resonances with enhanced sensitivity, *J. Comput. Phys.*, **486** (2023), 112131. http://doi.org/10.1016/j.jcp.2023.112131

27. W. Yin, H. Qi, P. Meng, Broad learning system with preprocessing to recover the scattering obstacles with far-field data, *Adv. Appl. Math. Mech.*, **15** (2023), 984–1000. https://doi.org/10.4208/aamm.OA-2021-0352

28. Y. Yin, W. Yin, P. Meng, H. Liu, The interior inverse scattering problem for a two-layered cavity using the Bayesian method, *Inverse Probl. Imag.*, **16** (2022), 673–690. https://doi.org/10.3934/ipi.2021069

29. Y. Yin, W. Yin, P. Meng, H. Liu, On a hybrid approach for recovering multiple obstacle, *Commun. Comput. Phys.*, **31** (2022), 869–892. https://doi.org/10.4208/cicp.OA-2021-0124

30. P. Meng, J. Zhuang, L. Zhou, W. Yin, D. Qi, Efficient synchronous retrieval of OAM modes and AT strength using multi-task neural networks, *Opt. Express*, **32** (2024), 7816–7831. http://doi.org/10.1364/OE.511098

31. P. Meng, X. Wang, W. Yin, ODE-RU: a dynamical system view on recurrent neural networks, *Electron. Res. Arch.*, **30** (2022), 257–271. http://doi.org/10.3934/era.2022014

32. Y. Gao, H. Liu, X. Wang, K. Zhang, A bayesian scheme for reconstructing obstacles in acoustic waveguides, *J. Sci. Comput.*, **97** (2023), 53. http://doi.org/10.1007/s10915-023-02368-2

33. D. Colton, R. Kress, Using fundamental solutions in inverse scattering, *Inverse Probl.*, **22** (2006), R49–R66. http://doi.org/10.1088/0266-5611/22/3/R01

34. F. Cakoni, D. Colton, *A qualitative approach to inverse scattering theory*, New York: Springer, 2014. http://doi.org/10.1007/978-1-4614-8827-9

35. J. Li, H. Liu, J. Zou, Multilevel linear sampling method for inverse scattering problems, *SIAM J. Sci. Comput.*, **30** (2008), 1228–1250. http://doi.org/10.1137/060674247

36. T. Arens, Why linear sampling works, *Inverse Probl.*, **20** (2004), 163–173. http://doi.org/10.1088/0266-5611/20/1/010

37. Y. Guo, P. Monk, D. Colton, The linear sampling method for sparse small aperture data, *Appl. Anal.*, **95** (2016), 1599–1615. http://doi.org/10.1080/00036811.2015.1065317

38. P. Meng, L. Su, W. Yin, S. Zhang, Solving a kind of inverse scattering problem of acoustic waves based on linear sampling method and neural network, *Alex. Eng. J.*, **59** (2020), 1451–1462. https://doi.org/10.1016/j.aej.2020.03.047